Hierarchical Mesoporous SnO_2 Nanosheets on Carbon Cloth: A Robust and Flexible Electrocatalyst for CO_2 Reduction with High Efficiency and Selectivity

Fengwang Li,[a,b] Lu Chen,[a] Gregory P. Knowles,[a] Douglas R. MacFarlane*[a,b] and Jie Zhang*[a,b]

Abstract: Electrochemical reduction of CO_2 into liquid fuels is a promising approach to achieve a carbon neutral energy cycle. However, conventional electrocatalysts usually suffer from low energy efficiency, poor selectivity and stability. Herein, a 3D hierarchical structure composed of mesoporous SnO_2 nanosheets on carbon cloth is proposed to efficiently and selectively electroreduce CO_2 to formate in aqueous media. The electrode is fabricated via a facile combination of hydrothermal reaction and calcination. It exhibits an unprecedented current density of ~50 mA cm^{-2} at a moderate overpotential (0.88 V) with high faradaic efficiency (89%), which is even larger than most gas diffusion electrodes. Additionally, the electrode also demonstrates flexibility and long–term stability. The superior performance is attributed to the robust and highly porous hierarchical structure, which provides a large surface area and facilitates charge and mass transfer. This study may open up new avenues to the design of 3D hierarchical electrodes with outstanding performance for the practical CO_2 reduction systems.

Producing carbon–based fuels or chemicals using the most abundant carbon source – CO_2 – is an attractive way to achieve a carbon neutral energy cycle.[1] Among different methods for this process, electrochemical reduction of CO_2 into fuels is a simple approach that can work under "green" conditions and in large scale, especially when driven by the electricity generated from renewable energy sources (*e.g.*, solar or wind).[2] However, due to the high stability of CO_2 and complicated multi–electron transfer kinetics, electrocatalytic CO_2 reduction reaction (CO_2RR) needs to overcome large energy barriers and can produce a mixture of products.[3] Recently, a variety of electrocatalysts or co–catalysts have been explored to activate this reaction, including metals,[4] metal oxides,[5] metal chalcogenides,[6] heteroatom doped carbon,[7] ionic liquids[8] and molecular complexes.[9] Despite these significant results, their activities still fall short of the practical requirement of high product yield at a low energy consumption in large–scale applications. It is still a great challenge and of significance to further investigate new strategies for steering CO_2RR toward desirable product(s) at lower overpotentials, higher activity and selectivity.

It is generally accepted that the electrocatalytic performance of an electroactive material is governed by at least three key factors:[10] (1) the intrinsic property of the active sites, which is determined by the chemical nature of the material; (2) the accessibility of the active sites by the reactive substrate, which can be manipulated by specifically designed electrode structures; and (3) the electron transfer efficiency, determined by the electrical conductivity of the catalyst itself and electron transport to the conductive catalyst support. The latter properties can be achieved by cultivating electrocatalysts in–situ on conductive supports (*e.g.*, nickel foam, stainless steel mesh, carbon cloth (CC), etc.) to ensure uniform growth of materials with nanostructural features able to generate hierarchical structures. Electrode structures of this kind are highly desirable since they not only possess large surface areas to increase the number of active sites, suppress the aggregation of active sites through anchoring effects, but also decrease the contact resistance and hence facilitate the electron transfer. This strategy has been considered as a highly promising avenue for applications in high performance energy conversion and storage systems, such as supercapacitors,[11] Li–ion batteries[12] and electrocatalysis.[13]

Despite the potential of hierarchical structures in the aforementioned applications, very little attention has been paid to their development in enhancing the performance of the electrocatalytic CO_2RR. On the other hand, even the state–of–the–art catalysts for this reaction show insufficient activity, *i.e.* the current densities are usually at the level of 1 – 10 mA cm^{-2} or less at the potentials of highest faradaic efficiency (FE). Therefore, it is urgent to boost the activity of the electrode material in order to efficiently implement CO_2RR in "artificial photosynthesis" devices. In addition, the electrodes should also have excellent mechanical strength and physical flexibility, which allow them to be integrated in various reactors to meet different requirements and standards. It is very recently reported that molecular cobalt porphyrin catalysts have been integrated into covalent organic frameworks by organic struts and immobilized on an electrode for improving the activity of its molecular counterpart.[14] Although this catalyst demonstrates enhanced performance, it remains very important to develop new and facile approaches for catalyzing CO_2RR.

Sn, as an inexpensive and Earth–abundant metal, has attracted intense interest as an electrocatalyst for CO_2RR because it can selectively catalyze CO_2 to formic acid (or formate at pH>3.8) with a maximum FE up to 90% at a moderate

[a] F. Li, L. Chen, Dr. G. P. Knowles, Prof. D. R. MacFarlane, Dr. J. Zhang
School of Chemistry, Monash University
Wellington Road, Clayton 3800, VIC, Australia
E–mail: jie.zhang@monash.edu, douglas.macfarlane@monash.edu
[b] F. Li, Prof. D. R. MacFarlane, Dr. J. Zhang
ARC Centre of Excellence for Electromaterials Science
Monash University, Wellington Road, Clayton 3800, VIC, Australia

Supporting information for this article is given via a link at the end of the document.

overpotential, especially when derived from its oxide.[4b,5c] However, the activity of Sn is too low for practical application (current density of a few mA cm^{-2} and only ~10 mA cm^{-2} even when loaded onto a carbon support).[3,5c] Herein, in order to improve the activity of Sn to an industry–desirable level, we propose a facile approach to grow porous SnO_2 nanosheets by preparing a SnS_2 nanosheet precursor on CC, followed by calcination in an air atmosphere. The as–prepared SnO_2 inherits the 2D nanosheet morphology of the SnS_2 precursor and also exhibits mesoporous structures created during the air calcination process. Thanks to this porous hierarchical feature, together with the conductive CC as 3D support and current collector, the electrode exhibits an unprecedented current response (~ 49 mA cm^{-2}) in the electroreduction of CO_2 to formate, with a very high FE (~90%) at a moderate overpotential in aqueous bicarbonate medium. Moreover, extended electrolysis also demonstrates the exceptional robustness of the catalyst.

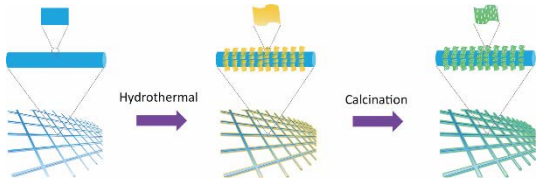

Scheme 1. Schematic illustration of the procedure for the synthesis of porous SnO_2 sheets on CC via hydrothermal reaction and subsequent calcination in the air atmosphere.

The porous hierarchical SnO_2 nanosheet material on CC (SnO_2/CC) was synthesized by a two–step process as schematically illustrated in **Scheme 1** (see Experimental Section in Supporting Information (SI) for details). Firstly, a strip of CC was immersed into an autoclave containing $SnCl_4$ and thioacetamide dissolved in isopropanol for hydrothermal growth of SnS_2 nanosheets on CC (SnS_2/CC). Secondly, the SnS_2 precursor was converted to mesoporous SnO_2 with retained nanosheet morphology via a simple calcination process in the air atmosphere. CC, as the supporting electrode, maintained essentially unchanged morphology, composition, electrical and mechanical properties during the calcination (Figure S1). In principle, this synthetic procedure is also applicable to larger–sized electrodes simply by increasing the size of the autoclave and also allows facile growth of catalysts on various other stable electrodes.

Scanning electron microscopy (SEM) was employed to study the microstructure of the as–grown SnS_2 and SnO_2 on CC. As shown in **Figure 1**a and b, densely packed SnS_2 nanosheets were formed uniformly and vertically on CC. The highly textured surface of the CC facilitates the nucleation and growth of SnS_2 with strong mechanical interactions. After calcination in air, the sulfide has been transformed to oxide, as revealed by the energy dispersive spectrum (Figure S2), while the morphology remains essentially unchanged as shown in Figure 1c. The thickness of this SnO_2 layer on CC is about 200 nm (Figure S3). Close observation (Figure 1d) reveals that the nanosheets contain numerous pores in the surface of the nanosheets, indicating that porous structures were formed during the calcination process. The retention of the nanosheet structure during calcination can be ascribed to the robust support of CC and the slow oxidation rate at a relatively low temperature.

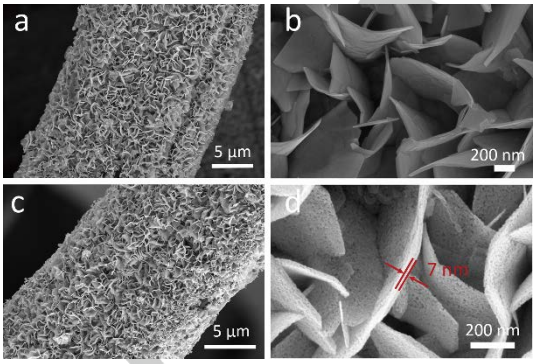

Figure 1. SEM images of SnS_2 nanosheets on CC (a, b) and porous SnO_2 nanosheets on CC (c, d).

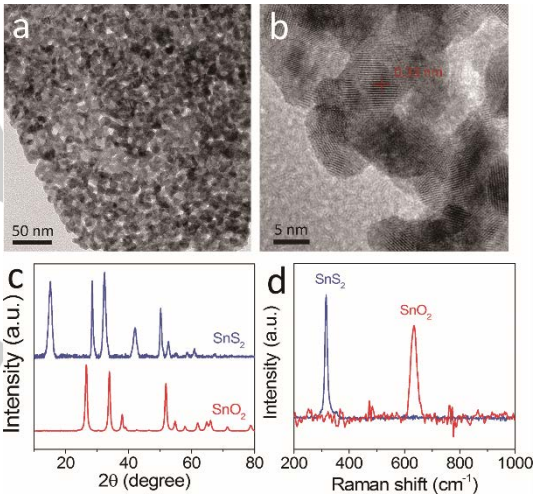

Figure 2. TEM (a) and HRTEM (b) images of porous SnO_2 nanosheets. XRD patterns (c) and Raman spectrum (d) of SnS_2 and SnO_2.

Further insight into the nanostructure of SnO_2/CC is presented by transmission electron microscopy (TEM). As revealed in **Figure 2**a, the SnO_2 nanosheets demonstrate a mesoporous structure with a pore size of ~ 5 nm, consistent with the high–resolution SEM observation. The high–resolution TEM (HRTEM) image in Figure 2b demonstrates the crystalline nature of SnO_2 nanosheets, and as denoted in the figure, the interplanar distance was measured to be 0.33 nm, which corresponds to the d–spacing of (110) plane of SnO_2.[15] By contrast, the SnS_2 nanosheets demonstrate a smooth surface (Figure S4). Crystal phase and chemical structures of SnS_2 and SnO_2 nanosheets are examined by X–ray diffractometry (XRD, Figure 2c) and Raman spectroscopy (Figure 2d). The XRD patterns can separately be indexed to hexagonal phase SnS_2 (JCPDS card No. 23–0677) and rutile tetragonal phase SnO_2 (JCPDS card No. 41–1445) while the peaks at 311 and 617 cm^{-2} are attributed to the A_{1g} mode

of SnS_2 and SnO_2, respectively.[16] These results confirm that SnS_2 has been successfully converted into phase–pure SnO_2 after calcination.

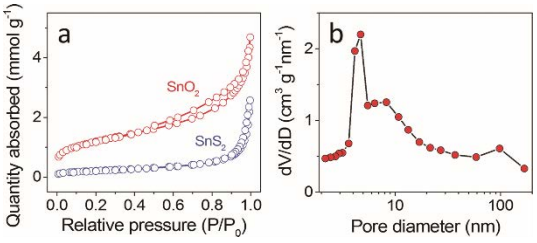

Figure 3. (a) Nitrogen adsorption–desorption isotherms for SnS_2 nanosheets and porous SnO_2. (b) The corresponding pore size distribution curve of SnO_2.

Measurements of isothermal (77 K) N_2 adsorption and desorption for neatly prepared SnS_2 and SnO_2 (**Figure 3**a) were made to characterize the surface area and porosity of the products. Each sample was found to exhibit a type 4 isotherm, while SnO_2 exhibiting substantially more micro and mesopore volume. The surface area of the porous SnO_2 (93.6 m^2 g^{-1}) was remarkably improved as compared to the non–porous SnS_2 (17.3 m^2 g^{-1}). The average pore diameter of the SnO_2 nanosheets is about 4~5 nm as measured by application of the Barrett–Joyner–Halenda method to the desorption data (Figure 3b), in excellent agreement with the TEM image in Figure 2a. The formation of the mesoporous structure could be due to the replacement of S^{2-} by smaller sized O^{2-} during calcination.[17] Importantly, all active sites are readily accessible to the reactant on a short timescale owing to the high mesoporosity and ultrathin thickness (less than 10 nm). Consequently, much enhanced electrocatalytic performance can be expected. Overall, the characterization data confirm that SnO_2/CC features a 3D hierarchical structure with high mesoporosity, which endows fast mass transport and electron transfer rates required for electrocatalytic applications.

SnO_2/CC can be directly used as the working electrode for electrocatalysis without extra substrates or binders. To examine SnO_2/CC electrode (mass loading of SnO_2 is 0.34 mg cm^{-2}, Figure S3) as an electrocatalyst for CO_2RR, constant potential electrolysis at a series of potentials were performed in a gas–tight H–cell with CO_2–saturated aqueous 0.5 M $NaHCO_3$ as electrolyte (pH 7.2). The gas products were determined by gas chromatography (GC) and the liquid products were characterized by ^{1}H NMR spectroscopy. The average current density of a one–hour electrolysis is plotted against potential in **Figure 4**a (i–t curve is shown in Figure S5). As expected, the kinetics of CO_2RR increased as the applied potential shifted negatively from –0.95 V to –1.8 V (vs. Ag/AgCl (3M KCl), all potentials hereafter are with respect to this reference). The dependence of FEs for the products on potential is plotted in Figure 4b, which indicates formate, H_2 and CO are the products with a combined FE of around 100% over the whole potential range and no other products were detected by NMR or GC. Results obtained from control experiments suggest CO_2 is the direct source of carbon in the liquid product (Figure S6). The selectivity towards formate and H_2 is strongly dependent on the applied potential while FE for CO (less than 10%) does not vary significantly with applied potential. At an applied potential of –0.95 V (corresponding to an overpotential of 0.23 V for formate), formate with a FE of ~18% was detected while H_2 is the dominant product. Both current density and FE for formate increase rapidly with increasingly negative potentials and FE for formate reaches a maximum of 89% at –1.6 V (overpotential of 0.88 V for formate) while delivering a current density of 49 mA cm^{-2}, after which it drops. This potential dependent formate selectivity has also been observed previously[4e,g,5c-e] and can be explained as follows: in the potential region at low CO_2/$HCOO^-$ overpotentials, HER is dominant since it is thermodynamically and kinetically more favourable. In the potential region at high CO_2/$HCOO^-$ overpotentials, kinetics of both CO_2 reduction and HER increase. However, HER regains dominance since CO_2 reduction is mass transport limited at high applied potential due to its low concentration in aqueous media (see Figure S7 and related discussion in SI).

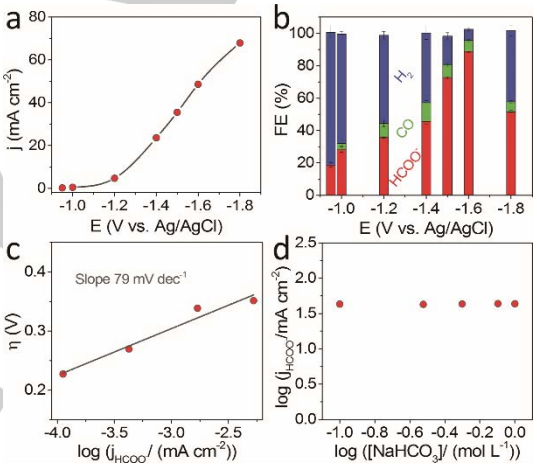

Figure 4. (a) Current density of SnO_2/CC electrode in CO_2–saturated 0.5 M $NaHCO_3$ solution at different applied potentials. (b) Corresponding FE for formate, CO and H_2. (c) Tafel plot of SnO_2/CC electrode. Partial current density for formate is calculated using surface area determined by BET. (d) Partial current density for formate vs. concentration of $NaHCO_3$. Partial current density is obtained by multiplying total current density with FE of formate in Figure S8.

Based on previous studies,[3,5c,7b] the following elementary steps are involved in the electrocatalytic reduction of CO_2 to formate:

$$CO_2\ (\text{solution}) \rightarrow CO_2\ (\text{ads}) \qquad \text{Eq. (1)}$$

$$CO_2\ (\text{ads}) + e^- \rightarrow CO_2 \cdot^-\ (\text{ads}) \qquad \text{Eq. (2)}$$

$$CO_2 \cdot^-\ (\text{ads}) + HCO_3^- \rightarrow HCOO \cdot\ (\text{ads}) + CO_3^{2-} \qquad \text{Eq. (3)}$$

$$HCOO \cdot\ (\text{ads}) + e^- \rightarrow HCOO^-(\text{ads}) \qquad \text{Eq. (4)}$$

$$HCOO^-(\text{ads}) \rightarrow HCOO^-(\text{solution}) \qquad \text{Eq. (5)}$$

In order to obtain an insight into the mechanism of CO_2 reduction on SnO_2/CC, Tafel analysis was performed (Figure 4c). A Tafel slope of 79 mV dec^{-1} is obtained on SnO_2/CC which is close to theoretical value of 59 mV for a rapid one–electron transfer step followed by a rate limiting chemical step.[3,18] This

implies that the formation of the adsorbed $CO_2^{\cdot-}$ intermediate (Eq. (2)) is not the rate determining step (RDS). Either Reaction (4) or (5) is not the RDS. Otherwise, a Tafel slope of about 39 and 30 mV dec^{-1}, respectively is predicted.[19] Therefore, Reaction (3) is most likely to be the RDS. Since the rate of formate formation is essentially independent on the concentration of $NaHCO_3$ (Figure 4d and S8), HCO_3^- involves in Reaction (3) is likely to be a surface adsorbed species whose coverage is not expected to alter appreciably when the concentration of $NaHCO_3$ is in the range of 0.1–1 M. However, it should be noted that this assignment of RDS has to be tentative giving the large uncertainty associated with experimentally determined Tafel slope value and the complexity of CO_2 reduction reaction. The presence of a competing HER and the fact that the aqueous bicarbonate medium is only weakly buffered are also expected to downplay the significance of the Tafel analysis.[3,18,19]

It is noteworthy to compare the performance between recently reported electrodes and our work. As shown in Table S1 in SI, our 3D hierarchical porous SnO_2/CC electrode outperforms almost all those reported, even gas diffusion electrodes, with respect to current density. The overpotential needed to reach the maximum FE for formate is also lower than most Sn or heteroatom–doped carbon based electrodes.

To evaluate the stability of the hierarchical porous SnO_2/CC electrode, electrolysis at fixed potential (–1.6 V) was carried out over an extended period. The current density was stable at ~50 mA cm^{-2} and the FE of formate remained essentially unchanged (87 ± 2%) over 24 h (**Figure 5**a and Figure S9). No morphology changed and the mesoporous structure was well reserved after the long–term electrolysis (Figure S10). New peaks attributed to metallic Sn emerged in the XRD pattern of the sample (Figure S10), indicating the active catalyst under catalytic turnover condition is Sn or Sn/SnO_x as reported by other groups.[4b,5c,20] Moreover, the electrode was also tested at different fold and twist states to see whether it can fulfil the demand of flexibility. As shown in Figure 5b, the electrodes after folding or twisting for 10 times present the same i–t trace as the original electrode, indicating the high flexibility and stability of the electrode. The aforementioned tests reveal that the SnO_2/CC electrode possesses superior stability and flexibility.

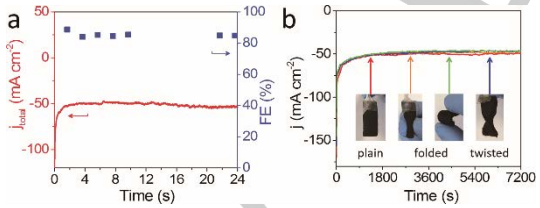

Figure 5. (a) i–t curve and FE for formate of SnO_2/CC electrode in CO_2–saturated 0.5 M $NaHCO_3$ solution at an applied potential of –1.6 V for 24 h. (b) i–t curves of SnO_2/CC electrode at –1.6 V after folding or twisting for 10 times.

In summary, we have synthesized a 3D hierarchical electrode composed of porous SnO_2 nanosheets on flexible carbon cloth via a facile combination of hydrothermal reaction and calcination. The as–prepared electrode can achieve a high current density at moderate overpotentials for the electroreduction of CO_2 to formate, with high selectivity and long–term stability. Such superior performance can be attributed to the following factors: (1) SnO_2, especially small particles of nanosize, has been proven to be an effective catalyst for electrochemical reduction of CO_2 to formate with high selectivity, which provides intrinsically active sites for the reaction; (2) the highly porous hierarchical structure delivers a large specific surface area, enlarging the contact surface between electrode and electrolyte, and facilitating the charge and mass transfer during the electrochemical reactions; (3) the good robustness of the hierarchical structures guarantees high stability of the electrocatalyst during long–term operation, even without any binders. This study opens up exciting new avenues to explore the design of 3D hierarchical electrodes with outstanding performance for the integration into practical devices.

Acknowledgements

This research was supported by the Australian Research Council (ARC) through the ARC Centre of Excellence for Electromaterials Science. DRM is grateful to the ARC for his Australian Laureate Fellowship. FL thanks Xiaolong Zhang for TGA measurements. The authors acknowledge the use of facilities within the Monash Centre for Electron Microscopy and the Monash X–Ray Platform.

Keywords: electrocatalysis • CO_2 reduction • nanostructures • nanosheet • 3D electrode

[1] A. Otto, T. Grube, S. Schiebahn, D. Stolten, *Energy Environ. Sci.* **2015**, *8*, 3283.

[2] a) J. Qiao, Y. Liu, F. Hong, J. Zhang, *Chem. Soc. Rev.* **2014**, *43*, 631; b) K. S. Lackner, *Science* **2003**, *300*, 1677.

[3] Y. Hori in *Modern Aspects of Electrochemistry*, *Vol. 42* (Eds.: C. G. Vayenas, R. E. White, M. E. Gamboa–Aldeco), Springer, New York, **2008**, pp. 89.

[4] a) K. P. Kuhl, T. Hatsukade, E. R. Cave, D. N. Abram, J. Kibsgaard, T. F. Jaramillo, *J. Am. Chem. Soc.* **2014**, *136*, 14107.; b) Y. Chen, M. W. Kanan, *J. Am. Chem. Soc.* **2012**, *134*, 1986; c) Y. Chen, C. W. Li, M. W. Kanan, *J. Am. Chem. Soc.* **2012**, *134*, 19969; d) X. Min, M. W. Kanan, *J. Am. Chem. Soc.* **2015**, *137*, 4701.; e) Q. Lu, J. Rosen, Y. Zhou, G. S. Hutchings, Y. C. Kimmel, J. G. Chen, F. Jiao, *Nature Commun.* **2014**, *5*, 3242; f) M. Ma, K. Djanashvili, W. A. Smith, *Angew. Chem.* **2016**, *128*, 6792; *Angew. Chem., Int. Ed.* **2016**, *55*, 6680; g) D. Kim, J. Resasco, Y. Yu, A. M. Asiri, P. Yang, *Nature Commun.* **2014**, *5*, 4948; h) Y. Zhao, C. Wang, G. G. Wallace, *J. Mater. Chem. A* **2016**, *4*, 10710; h) M. Ma, B. J. Trześniewski, J. Xie, W. A. Smith, *Angew. Chem.* **2016**, *128*, 9900; *Angew. Chem., Int. Ed.* **2016**, *55*, 9748.

[5] a) Y. Oh, H. Vrubel, S. Guidoux, X. Hu, *Chem. Commun.* **2014**, *50*, 3878; b) C. W. Li, M. W. Kanan, *J. Am. Chem. Soc.* **2012**, *134*, 7231; c) S. Zhang, P. Kang, T. J. Meyer, *J. Am. Chem. Soc.* **2014**, *136*, 1734; d) S. Gao, X. Jiao, Z. Sun, W. Zhang, Y. Sun, C. Wang, Q. Hu, X. Zu, F. Yang, S. Yang, L. Liang, J. Wu, Y. Xie, *Angew. Chem.* **2016**, *128*, 708; *Angew. Chem., Int. Ed.* **2016**, *55*, 698; e) S. Gao, Y. Lin, X. Jiao, Y. Sun, Q. Luo, W. Zhang, D. Li, J. Yang, Y. Xie, *Nature* **2016**, *529*, 68.

[6] a) X. Sun, Q. Zhu, X. Kang, H. Liu, Q. Qian, Z. Zhang, B. Han, *Angew. Chem.* **2016**, *128*, 6883; *Angew. Chem., Int. Ed.* **2016**, *55*, 6771; b) F. Li, S. F. Zhao, L. Chen, A. Khan, D. R. MacFarlane, J. Zhang, *Energy Environ. Sci.* **2016**, *9*, 216; c) M. Asadi, B. Kumar, A. Behranginia, B. A. Rosen, A. Baskin, N. Repnin, D. Pisasale, P. Phillips, W. Zhu, R. Haasch, R. F. Klie, P. Kral, J. Abiade, A. Salehi–Khojin, *Nature Commun.* **2014**, *5*, 4470.

[7] a) J. Wu, R. M. Yadav, M. Liu, P. P. Sharma, C. S. Tiwary, L. Ma, X. Zou, X. D. Zhou, B. I. Yakobson, J. Lou, *ACS Nano* **2015**, *9*, 5364; b) H. Wang, Y. Chen, X. Hou, C. Ma, T. Tan, *Green Chem.* **2016**, *18*, 3250; c) Y. Liu, S. Chen, X. Quan, H. Yu, *J. Am. Chem. Soc.* **2015**, *137*, 11631; d) B. Kumar, M. Asadi, D. Pisasale, S. Sinha–Ray, B. A. Rosen, R. Haasch, J. Abiade, A. L. Yarin, A. Salehi–Khojin, *Nature Commun.* **2013**, *4, 2819*; e) S. Narayanaru, A. N. Mohammed, V. V. Thazhe, S. Krishnamurty, K. L. Phani, *Chem. Commun.* **2015**, *51*, 16061.

[8] a) N. Hollingsworth, S. F. R. Taylor, M. T. Galante, J. Jacquemin, C. Longo, K. B. Holt, N. H. de Leeuw, C. Hardacre, *Angew. Chem.* **2015**, *127*, 14370; *Angew. Chem., Int. Ed.* **2015**, *54*, 14164; b) B. A. Rosen, A. Salehi–Khojin, M. R. Thorson, W. Zhu, D. T. Whipple, P. J. Kenis, R. I. Masel, *Science* **2011**, *334*, 643; c) Q. Zhu, J. Ma, X. Kang, X. Sun, H. Liu, J. Hu, Z. Liu, B. Han, *Angew. Chem.* **2016**, *128*, 9158; *Angew. Chem., Int. Ed.* **2016**, *55*, 9012.

[9] a) A. Chapovetsky, T. H. Do, R. Haiges, M. K. Takase, S. C. Marinescu, *J. Am. Chem. Soc.* **2016**, *138*, 5765; b) C. W. Machan, M. D. Sampson, C. P. Kubiak, *J. Am. Chem. Soc.* **2015**, *137*, 8564; c) C. Costentin, S. Drouet, M. Robert, J. M. Saveant, *Science* **2012**, *338*, 90.

[10] J. Lai, S. Li, F. Wu, M. Saqib, R. Luque, G. Xu, *Energy Environ. Sci.* **2016**, *9*, 1210.

[11] a) Y. Guo, L. Yu, C. Y. Wang, Z. Lin, X. W. Lou, *Adv. Funct. Mater.* **2015**, *25*, 5184; b) L. Q. Mai, F. Yang, Y. L. Zhao, X. Xu, L. Xu, Y. Z. Luo, *Nature Commun.* **2011**, *2*, 381.

[12] a) F. Zhou, S. Xin, H. W. Liang, L. T. Song, S. H. Yu, *Angew. Chem.* **2014**, *126*, 11736; *Angew. Chem., Int. Ed.* **2014**, *53*, 11552; b) R. Zou, Z. Zhang, M. F. Yuen, M. Sun, J. Hu, C. S. Lee, W. Zhang, *NPG Asia Mater.* **2015**, *7*, e195.

[13] a) D. Kong, H. Wang, Z. Lu, Y. Cui, *J. Am. Chem. Soc.* **2014**, *136*, 4897; b) T. Y. Ma, S. Dai, M. Jaroniec, S. Z. Qiao, *J. Am. Chem. Soc.* **2014**, *136*, 13925; c) A. L. Wang, X. J. He, X. F. Lu, H. Xu, Y. X. Tong, G. R. Li, *Angew. Chem.* **2015**, *127*, 3740; *Angew. Chem., Int. Ed.* **2015**, *54*, 3669; d) J. Miao, F. X. Xiao, H. B. Yang, S. Y. Khoo, J. Chen, Z. Fan, Y. Y. Hsu, H. M. Chen, H. Zhang, B. Liu, *Sci. Adv.* **2015**, *1*, e1500259.

[14] S. Lin, C. S. Diercks, Y. B. Zhang, N. Kornienko, E. M. Nichols, Y. Zhao, A. R. Paris, D. Kim, P. Yang, O. M. Yaghi, C. J. Chang, *Science* **2015**, *349*, 1208.

[15] Y. Sun, F. Lei, S. Gao, B. Pan, J. Zhou, Y. Xie, *Angew. Chem.* **2013**, *125*, 10763; *Angew. Chem., Int. Ed.* **2013**, *52*, 10569.

[16] a) Y. Zheng, T. Zhou, C. Zhang, J. Mao, H. Liu, Z. Guo, *Angew. Chem.* **2016**, *128*, 3469; *Angew. Chem., Int. Ed.* **2016**, *55*, 3408; b) B. Luo, Y. Fang, B. Wang, J. Zhou, H. Song, L. Zhi, *Energy Environ. Sci.* **2012**, *5*, 5226.

[17] Q. Wang, D. Wang, M. Wu, B. Liu, J. Chen, T. Wang, J. Chen, *J. Phys. Chem. Solids* **2011**, *72*, 630.

[18] E. Gileadi, *Electrode Kinetics for Chemists, Engineers, and Materials Scientists*, Wiley-VCH, New York, **1993**.

[19] S. Fletcher, *J. Solid State Electrochem.* **2009**, *13*, 537.

[20] M. F. Baruch, J. E. Pander, J. L. White, A. B. Bocarsly, *ACS Catal.* **2015**, *5*, 3148; A. Dutta, A. Kuzume, M. Rahaman, S. Vesztergom, P. Broekmann, *ACS Catal.* **2015**, *5*, 7498.

Entry for the Table of Contents

COMMUNICATION

Mesoporous SnO_2 nanosheets in–situ grown on carbon cloth is used as a robust and flexible electrode for electroreducing CO_2 to formate with high efficiency and selectivity. The superior performance is due to the hierarchical structure, which provides high surface area, fast charge and mass transport and robustness. This electrode holds potential to be used in practical "artificial photosynthesis" devices.

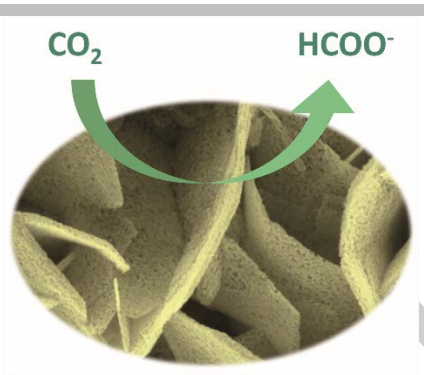

Fengwang Li, Lu Chen, Gregory Knowles, Douglas R. MacFarlane, Jie Zhang**

Page No. – Page No.

Hierarchical Mesoporous SnO_2 Nanosheets on Carbon Cloth: A Robust and Flexible Electrocatalyst for CO_2 Reduction with High Efficiency and Selectivity

1. Experimental Section

Materials and Apparatus: $NaHCO_3$ (ACS grade), dimethylsulfoxide (DMSO), acetone, isopropanol and ethanol were purchased from Merck; thioacetamide, anhydrous $SnCl_4$ and Nafion (5 wt%) were purchased from Sigma–Aldrich; carbon cloth was from Tsukuba Materials Information Laboratory. All the chemicals were used without further purification. All the aqueous solutions were prepared with Milli Q water (18.2 MΩ cm). Carbon cloth was washed with water and acetone thoroughly prior to use.

Raman spectra was obtained using a Renishaw inVia Microscope with a 514 nm laser source and X–ray Diffraction (XRD) data were collected with a Bruker D2 PHASER powder diffractometer (Cu K_α radiation, λ = 0.15406 nm). Thermogravimetric analysis (TGA) was conducted on TGA/DSC 3+ (METTLER TOLEDO) in air at a heating rate of 10 °C min^{-1} from 100 to 900 °C. The surface area and pore diameter distribution of the SnS_2 nanosheets and porous SnO_2 nanosheets were tested by nitrogen adsorption (P/P_0 0.05–0.3) and desorption (P/P_0 0.99–0.17), isothermal data analysis, respectively, at 77K on a Micromeritics TriStar 3020 instrument. The surface area of the products was estimated by method of Brunauer–Emmett–Teller (BET,) and the estimation of the distribution of mesopores within SnO_2 was made by application of the Barrett–Joyner–Halenda (BJH) method to the desorption data. Transmission electron microscopic (TEM) images were collected on a FEI Tecnai G2 T20 TWIN TEM. Scanning electron microscopic (SEM) images and energy dispersive spectrum (EDS) were recorded on a FEI Nova NanoSEM 450 FEG SEM equipped with Bruker Quantax 400 X–ray analysis system. ^1H NMR experiments were undertaken with a Bruker DRX400 spectrometer at frequencies of 400.2 MHz. Gas chromatography (GC) was performed with an Agilent 7820 A gas chromatography system equipped with a HP–plot molesieve (5A) column and a thermal conductivity detector (TCD). The carrier gas was helium (99.99%) for CO analysis while nitrogen (99.99%) was used as carrier gas for H_2 analysis. The retention times

were compared with known compounds. All the electrochemical experiments were conducted on a CHI 760D electrochemical workstation (CH Instruments, Austin, Texas, USA) at room temperature (22 ± 2 °C).

Synthesis of SnS_2/CC and SnO_2/CC: Thioacetamide (0.016 g) and $SnCl_4$ (7 μL) were added to a 15 mL Teflon–lined stainless steel autoclave containing 10 mL isopropanol and sonicated until all the materials were dissolved. Afterwards, a piece of carbon cloth (3 cm × 1 cm) was placed standing against the wall of the autoclave, sealed tightly, and heated at 180 °C for 24 h. After cooling to room temperature naturally, the carbon cloth was taken out by a tweezer, mildly sonicated in water for 1 min, rinsed with water and ethanol for at least 5 times and then dried in the oven at 80 °C overnight. To prepare the SnO_2/CC electrode, the as–prepared SnS_2/CC was placed in a quartz boat, and calcined at 500 °C for 2 h in a furnace under the air atmosphere. After cooling to room temperature, SnO_2/CC was obtained. SnS_2 nanosheets and porous SnO_2 nanosheets for Nitrogen adsorption/desorption, XRD, Raman analysis were prepared without putting carbon cloth in the autoclave.

CO_2 Reduction Electrolysis and Product Analysis: Electrolysis was performed in a gas–tight H–type electrochemical cell with a glass frit as the separator. Each compartment contained 10 mL of 0.5 M $NaHCO_3$ electrolyte and approximately 22.5 mL headspace. A carbon rod was used as the counter electrode, an Ag/AgCl (3 M KCl) as reference electrode and a piece of SnO_2/CC as working electrode, respectively. Before electrolysis, the cell was degassed by bubbling CO_2 gas for at least 30 min. The solutions in both compartment were stirred during electrolysis. After the electrolysis, a small fraction of the cell's head space products (200 μL) was sampled by gas–tight syringe and analyzed by GC. Afterwards, 0.6 mL electrolyte was taken out and mixed with 0.1 mL D_2O and 0.1 mL DMSO (diluted to 100 ppm (v/v) by water prior to use) added as an internal standard. The samples were quantitatively analyzed by ^1H NMR. The electrode after electrolysis was rinsed with water thoroughly, dried and used for

morphology analysis. In order to prepare samples for XRD analysis, the electrode was quickly rinsed with water immediately after the electrolysis and sonicated in ethanol to dissolve the active material and dried under vacuum.

2. Supplementary Figures

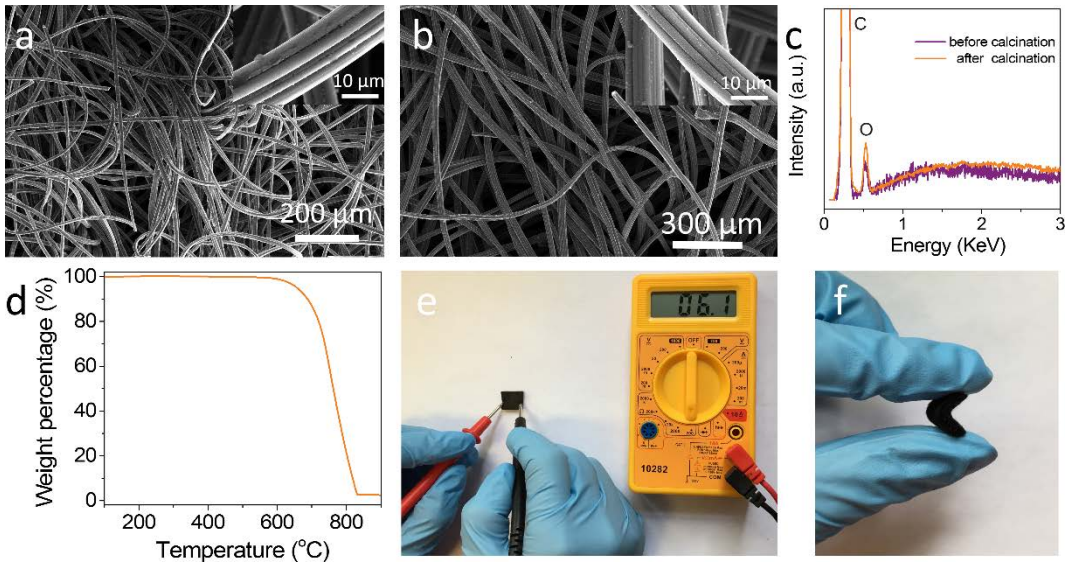

Figure S1. SEM images of bare CC before (a) and after (b) calcination. Inserts are the high–magnification images. (c) EDS of CC before and after calcination. (d) TGA curve of bare CC in air. (e) Resistance test of CC after calcination. Measurement range in the multimeter is 200 Ω. The resistance value of the same CC before calcination was 4.7 Ω. (f) A bent CC after calcination showing the undamaged flexibility.

Directly heating the pristine CC under the same conditions used for the synthesis of SnO_2/CC carbon cloth was performed to check whether CC could be destroyed by the calcination. As shown in Figure S1a and b, the morphology of CC keeps essentially unchanged except that the surface become rough after calcination. Oxygen content increases a bit, from 0.43% in pristine CC to 0.67% in the heated one, as suggested by EDS (Figure S1c). TGA also confirms that CC is stable under air at 500 °C (Figure S1d). Furthermore, electrical or mechanical properties of CC, which are the most important properties for electrochemical applications, do not seem to be affected appreciably during the calcination process (Figure S1e and f).

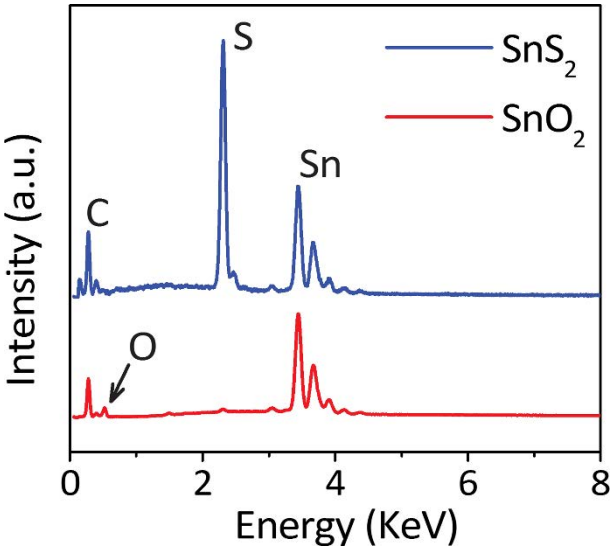

Figure S2. EDS of SnS_2/CC and SnO_2/CC.

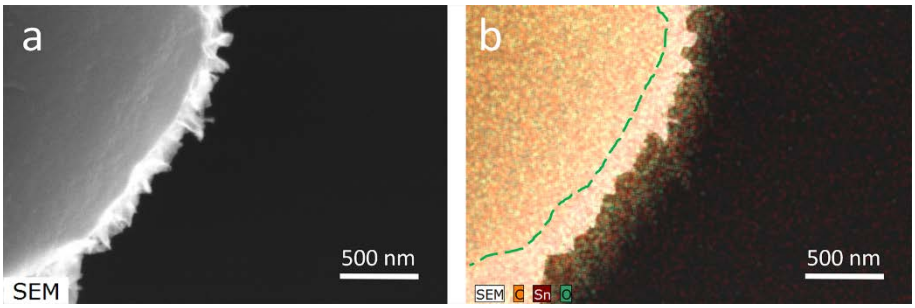

Figure S3. SEM image (a) and corresponding EDS mapping result (b) of SnO_2/CC. The green dash line indicates the boundary of carbon cloth. The thickness of SnO_2 is about 200 nm.

The mass loading of SnO_2 on CC was also quantified. For this, the weight difference of the CC before and after the loading of SnO_2 was measured by a high–precision micro balance (Sartorius, max weight 31 g, d = 0.001 mg) after substantial drying, giving the fact that the weight of bare CC did not change during the calcination process (Figure S1d). The data are shown below.

	m_{CC} (mg)	$m_{SnO2/CC}$ (mg)	m_{SnO2} (mg)	$m_{average}$ (mg)
Sample 1	114.191	115.266	1.075	1.024
Sample 2	112.992	113.845	0.853	
Sample 3	118.982	120.127	1.145	

The geometric area of the sample is 3 cm^2; therefore, the loading of SnO_2 is 0.34 mg cm^{-2}.

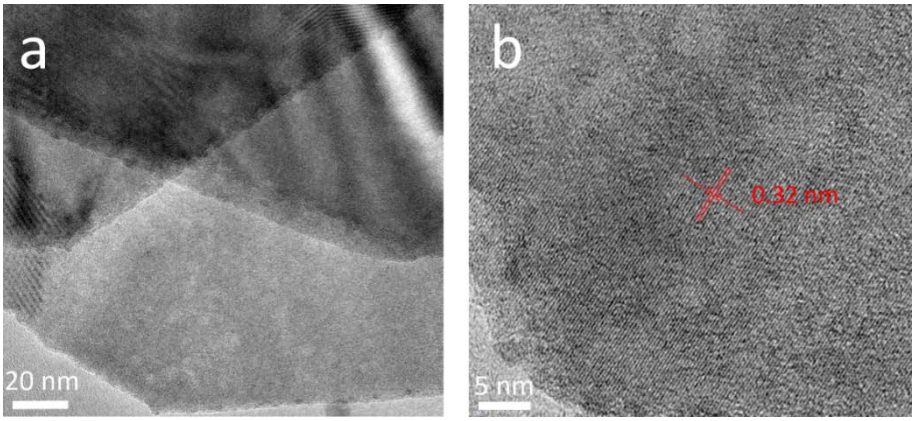

Figure S4. TEM (a) and HRTEM (b) images of SnS_2 nanosheet, showing a smooth surface. As denoted in (b), the interplanar distance is measured to be 0.32 nm, which corresponds to the d–spacing of (100) plane of SnS_2.

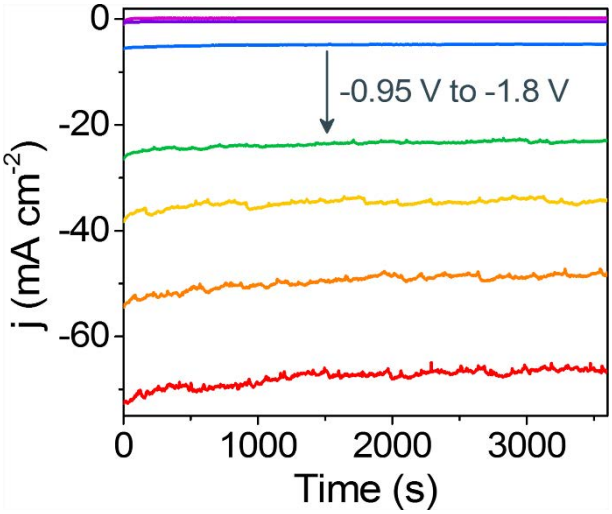

Figure S5. Total current density *vs.* time curve during electrolysis at different applied potentials.

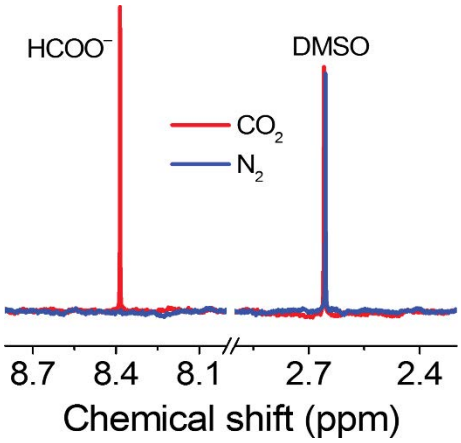

Figure S6. Representative NMR spectra of the electrolyte after electrolysis at −1.6 V (vs. Ag/AgCl) for SnS_2/rGO material in CO_2 (red) and N_2 (blue) saturated 0.5 M $NaHCO_3$ electrolyte. DMSO is used as an internal standard to quantify $HCOO^-$.

Electrolysis under N_2 or CO_2 saturated 0.5 M $NaHCO_3$ solution were conducted and the liquid products were analyzed by NMR. It is clear to see that no formate was produced if the electrolyte solution is saturated with N_2, which rules out HCO_3^- being the direct source of carbon.

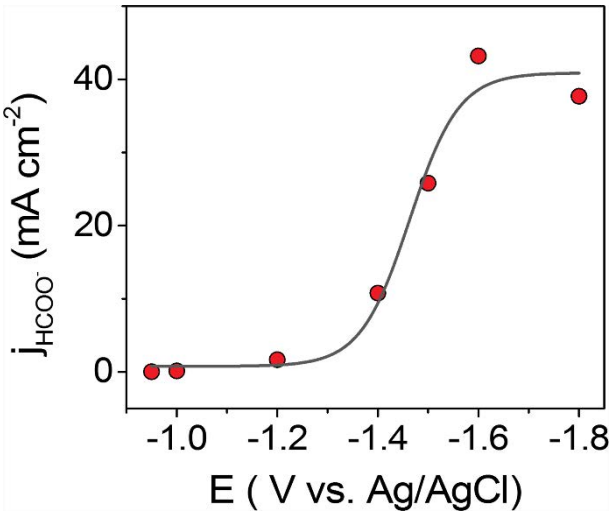

Figure S7. Partial current density for formate at different applied potentials. The data were obtained by multiplying the total current density for electrolysis by the FE of formate.

The dependence of partial current density of formate on potential is instructive to evaluate the role of mass transport in CO_2 reduction. This $j_{HCOO^-} - E$ curve is plotted in Figure S7 and a clear sigmoidal shape is evident. Although we cannot conclude the mass transport solely based on the sigmoidal shape of this curve, mass transport is likely playing an important role in this process.

We also estimated the mass transport current based on theoretical calculation. In our experiment, convection (by string the solution with a magnetic stir bar) was introduced to enhance the mass transport rate during electrolysis. The following equation was used to estimate the mass transport limited current density (j_{lim}),[1]

$$j_{\mathrm{lim}} = nF\frac{D}{\delta}c$$

where n represents the number of electrons transferred and F is the Faraday's constant. D and c is the diffusion coefficient and concentration of the reactant, respectively. δ is the "diffusion" layer thickness, which is affected by stirring speed. Since mass transport is not well–defined under bulk electrolysis conditions, it is difficult to calculate δ value accurately. Thus, δ value

is roughly estimated using the following equation, that is applied to a rotating disc electrode under laminar flow conditions:[1]

$$\delta = 1.61 D^{\frac{1}{3}} \omega^{-\frac{1}{2}} \nu^{\frac{1}{6}}$$

where D, ω and ν is the diffusion coefficient of reactant, rotation speed and kinematic viscosity of the electrolyte, respectively. The values of these parameters are listed below:

n	F (C mol^{-1})	D (m^2 s^{-1})	c (mol m^{-3})	ν (m^2 s)
2	96485	1.91×10^{-9}	34	1.09×10^{-6}

A j_{lim} value of 45 mA cm^{-2} can be obtained using a moderate rotation speed 500 rpm (ω = 52.4 s^{-1}). This value is comparable to 40 mA cm^{-2} found experimentally. Given the large uncertainty associated with the estimated j_{lim}, it is reasonable to conclude that CO_2 reduction could be mass–transport controlled under our experimental condition.

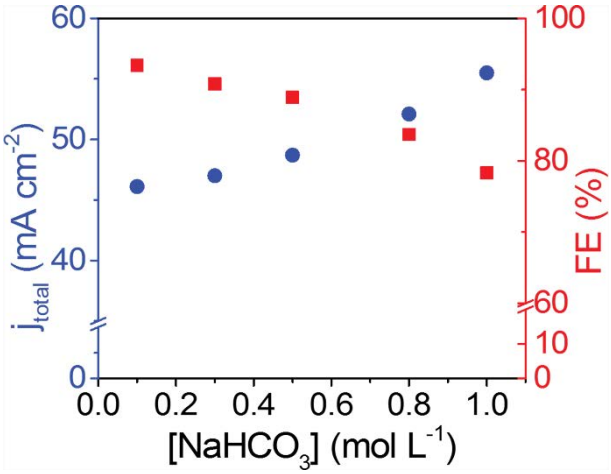

Figure S8. Total current density and FE for formate for SnO_2/CC electrode in $NaHCO_3$ solutions with different concentration (saturated with CO_2) at –1.6 V vs. Ag/AgCl. In these experiments, the total ionic strength was not controlled since it is not straightforward to find an innocent supporting electrolyte for this purpose.

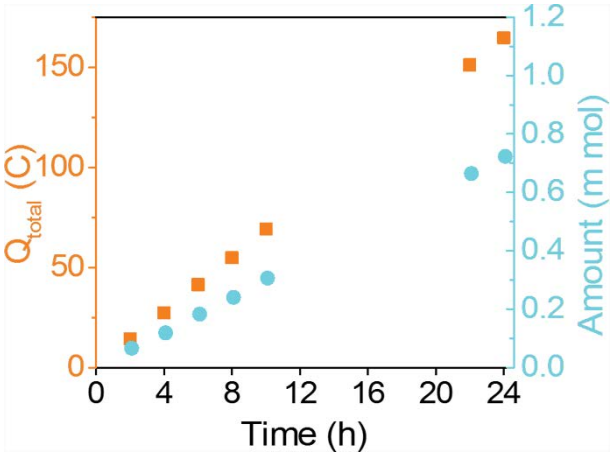

Figure S9. Charge consumed and amount of formate generated during the electrolysis process. The electrolysis was conducted continuously using a SnO_2/CC electrode in CO_2–saturated 0.5 M $NaHCO_3$ solution at an applied potential of –1.6 V for 24 h. 0.5 mL electrolyte solutions were taken every 2 h in the first 10 h and the last 4h for NMR quantification.

Both the amount of formate and electricity increase linearly with time (Figure S9), and the FE of formate remains essentially unchanged (87 ± 2%) (Figure 5a)

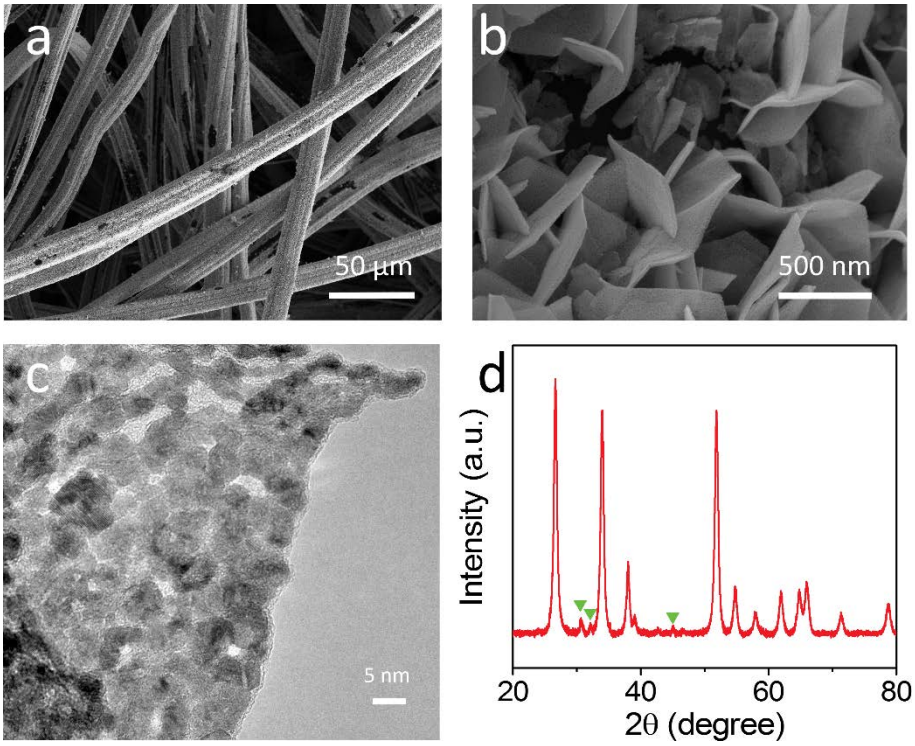

Figure S10. Low (a) and high (b) magnification SEM images and TEM (c) image of SnO_2/CC after electrolysis. (c) XRD pattern of SnO_2 after electrolysis. In addition to the dominate peaks of rutile tetragonal phase SnO_2 (JCPDS card No. 41–1445), three new peaks emerge, as indicated by green arrows, which can be indexed to the (200), (101), (211) phases of metallic Sn (JCPDS card No. 04–0673), respectively.

The formal potential E°' for $SnO_2 + 4\ H^+ + 4\ e^- \rightarrow Sn + 2\ H_2O$ is -0.543 V (vs. NHE, pH 7.2, 25 °C). In principle, all SnO_x should be reduced to metallic Sn under our experimental conditions. However, it has been confirmed in literatures[2,3] that some SnO_x is present in a metastable state in a wide potential region that is far more negative than the formal potential. Therefore, the composition of Sn/SnO_x is not expected to vary significantly in the potential range of our interest.

3. Supplementary Table

Table S1. Comparison of the electrocatalytic performance for reducing CO_2 to formate on different electrodes and electrolytes.

Electrode	Electrolyte	E_{app} (V)[a]	j_{total}[b] (mA cm^{-2})	$FE_{formate}$[c]	Ref.
Sn/SnO_x	0.5 M $NaHCO_3$	–0.7 V vs. RHE	~2	~38%	[4]
Sn foil	0.1 M $KHCO_3$	–1.8 V vs. Ag/AgCl	2.5	91%	[5]
SnO_2	0.5 M NaOH (pH 10.2)	–0.6 V vs. RHE	3.5	67.6%	[6]
SnO_2 GDE[d]	0.5 M $KHCO_3$	–1.7 V vs. NHE	6	68%	[7]
SnO_2/graphene	0.1 M $NaHCO_3$	–1.8 V vs. SCE[e]	10.2	93.6%	[8]
Sn GDE	0.5 M $KHCO_3$	–1.8 V vs. Ag/AgCl	13.45	72.99%	[9]
Electrodeposited Sn	0.1 M $KHCO_3$	–1.4 V vs. SCE	15	91%	[10]
Sn dendrite	0.1 M $KHCO_3$	–1.36 V vs. RHE[f]	17.1	71.6%	[11]
Sn GDE	0.5 M $KHCO_3$	–1.8 V vs. Ag/AgCl	22.2	78.6%	[12]
Sn foam	0.1 M $NaHCO_3$	–2.0 V vs. Ag/AgCl	23.5	90%	[13]
Sn/Nafion GDE	0.5 M $NaHCO_3$	–1.6 V vs. NHE[g]	27	70%	[14]
Sn foil	0.5 M $KHCO_3$	–2.0 V vs. SCE	28	63.5%	[15]
Sn–Pb alloy on carbon cloth	0.5 M $KHCO_3$	–2.0 V vs. Ag/AgCl	57.3	79.8%	[16]
Boron–doped graphene	0.1 M $KHCO_3$	–1.4 V vs. SCE	~1.5	66%	[17]
Nitrogen–doped graphene	0.5 M $KHCO_3$	–0.84 V vs. RHE	7.5	73%	[18]
PEI–NGCNT[h]	0.1 M $KHCO_3$	–1.8 V vs. SCE	9.5	87%	[19]
Co_3O_4	0.1 M $KHCO_3$	–0.88 V vs. SCE	0.68	64.3%	[20]
Partially oxidized Co layers	0.1 M Na_2SO_4	–0.85 V vs. SCE	10.59	90.1%	[21]
Ag	$[P_{66614}][124Triz]/H_2O/AcN$[i]	–0.7 V vs. Ag/Ag^+	n.a.[j]	95%	[22]
Pb	$[BmimPF_6]/H_2O/AcN$[k]	–2.3 V vs. Ag/Ag^+	41	91.6%	[23]
Sn	$[BmimPF_6]/H_2O/AcN$	–2.3 V vs. Ag/Ag^+	34.6	92.0%	[23]
Porous SnO_2/carbon cloth	0.5 M $NaHCO_3$	–1.6 V vs. Ag/AgCl	48.6	89%	This work

[a] Applied potential at the maximum faradaic efficiency (FE). [b] Total current density at the maximum FE. [c] Maximum FE of formate. [d] Gas diffusion electrode. [e] Saturated calomel electrode. [f] Reversible hydrogen electrode. [g] Normal hydrogen electrode. [h] Polyethylenimine/nitrogen–doped carbon nanotube. [i] $[P_{66614}][124Triz]$: Trihexyltetradecylphosphonium 1,2,4–triazole ionic liquid; can: acetonitrile. [j] not available. [k] $[BmimPF_6]$: 1–Butyl–3–methylimidazolium hexafluorophosphate.

References

[1] A. J. Bard, L. R. Faulkner, *Electrochemical Methods: Fundamentals and Applications*, Wiley, **2000**.
[2] M. F. Baruch, J. E. Pander, J. L. White, A. B. Bocarsly, *ACS Catal.* **2015**, *5*, 3148.
[3] A. Dutta, A. Kuzume, M. Rahaman, S. Vesztergom, P. Broekmann, *ACS Catal.* **2015**, *5*, 7498.
[4] Y. Chen, M. W. Kanan, *J. Am. Chem. Soc.* **2012**, *134*, 1986.
[5] W. Lv, R. Zhang, P. Gao, L. Lei, *J. Power Sources* **2014**, *253*, 276.
[6] S. Lee, J. D. Ocon, Y. I. Son, J. Lee, *J. Phys. Chem. C* **2015**, *119*, 4884.
[7] Y. Fu, Y. Liu, Y. Li, J. Qiao, X. D. Zhou, *ECS Trans.* **2015**, *66*, 53.
[8] S. Zhang, P. Kang, T. J. Meyer, *J. Am. Chem. Soc.* **2014**, *136*, 1734.
[9] Q. Wang, H. Dong, H. Yu, *RSC Adv.* **2014**, *4*, 59970.
[10] C. Zhao, J. Wang, *Chem. Eng. J.* **2016**, *293*, 161.
[11] D. H. Won, C. H. Choi, J. Chung, M. W. Chung, E. H. Kim, S. I. Woo, *ChemSusChem* **2015**, *8*, 3092.
[12] Q. Wang, H. Dong, H. Yu, *J. Power Sources* **2014**, *271*, 278.
[13] D. Du, R. Lan, J. Humphreys, S. Sengodan, K. Xie, H. Wang, S. Tao *ChemistrySelect* **2016**, *1*, 1711.
[14] G. K. S. Prakash, F. A. Viva, G. A. Olah, *J. Power Sources* **2013**, *223*, 68.
[15] J. Wu, F. Risalvato, X. D. Zhou, *ECS Trans.* **2012**, *41*, 49.
[16] S. Y. Choi, S. K. Jeong, H. J. Kim, I. H. Baek, K. T. Park, *ACS Sustain. Chem. Eng.* **2016**, *4*, 1311.
[17] S. Narayanaru, A. N. Mohammed, V. V. Thazhe, S. Krishnamurty, K. L. Phani, *Chem. Commun.* **2015**, *51*, 16061.
[18] H. Wang, Y. Chen, X. Hou, C. Ma, T. Tan, *Green Chem.* **2016**, *18*, 3250.
[19] S. Zhang, P. Kang, S. Ubnoske, M. K. Brennaman, N. Song, R. L. House, J. T. Glass, T. J. Meyer, *J. Am. Chem. Soc.* **2014**, *136*, 7845.
[20] S. Gao, X. Jiao, Z. Sun, W. Zhang, Y. Sun, C. Wang, Q. Hu, X. Zu, F. Yang, S. Yang, L. Liang, J. Wu, Y. Xie, *Angew. Chem.* **2016**, *128*, 708; *Angew. Chem., Int. Ed.* **2016**, *55*, 698.
[21] S. Gao, Y. Lin, X. Jiao, Y. Sun, Q. Luo, W. Zhang, D. Li, J. Yang, Y. Xie, *Nature* **2016**, *529*, 68.
[22] N. Hollingsworth, S. F. R. Taylor, M. T. Galante, J. Jacquemin, C. Longo, K. B. Holt, N. H. de Leeuw, C. Hardacre, *Angew. Chem.* **2015**, *127*, 14370; *Angew. Chem., Int. Ed.* **2015**, *54*, 14164.
[23] Q. Zhu, J. Ma, X. Kang, X. Sun, H. Liu, J. Hu, Z. Liu, B. Han, *Angew. Chem.* **2016**, *128*, 9158; *Angew. Chem., Int. Ed.* **2016**, *55*, 9012.